Stanford Exploration Project, Report 113, July 8, 2003, pages 145–157

Phase-shift migration of approximate zero-offset teleseismic data

Jeff Shragge[1]

ABSTRACT

A hybrid of traditional survey-sinking migration is derived that is applicable to teleseismic wavefields. To reconfigure teleseismic data to an approximate equivalent of zero-offset, an adjoint linear moveout shift is applied. This transformation enables the straightforward development of phase-shift operators to downward continue the modified teleseismic data. This method also affords an opportunity for imaging earth structure with a variety of forward- and backscattered modes through appropriate choices of wavefield velocities. This method is applied to a synthetic teleseismic data set, and several migration results are presented to demonstrate its effectiveness.

INTRODUCTION

The use of idealized plane-wave sources in exploration seismic imaging is well documented (Claerbout, 2001). One situation where plane-wave sources are often realized is in imaging with earthquake waves recorded at large epicentral distances (i.e. teleseismic distances). Many advances in teleseismic imaging have stemmed from adapting existing seismic exploration techniques to the teleseismic context. In particular, much recent effort has been centered on reconfiguring multi-dimensional Kirchhoff-based migration/inversion formulations for teleseismic plane-wave sources and acquisition geometry (Bostock et al., 2001).

Multi-dimensional wave-equation migration methods are not applied widely in teleseismic imaging. Although the advantages of wave equation-based methods over their Kirchhoff counterparts are known to explorationists, two issues persistently hinder their use in the teleseismic community. One problem is that Fourier-based methods are difficult to apply to data of non-uniform spacing. In practice, this is often observed because of practical limitations in acquisition. A second issue is that the geometry of teleseismic sources and data needs to be reconciled with the geometry of traditional pre- and post-stack migration formulations. Hence, both of these issues must be addressed before wave-equation migration algorithms are applied.

The aim of this paper is to show that, with only minor adjustments, traditional wave-equation migration is readily applicable to teleseismic wavefields (i.e. by accounting for the effects of upward propagating plane-wave sources). This paper specifically addresses the second issue by demonstrating that the application of an adjoint linear moveout (LMO) operator successfully reconfigures teleseismic data to an approximate equivalent of traditional zero-offset

[1]**email:** jeff@sep.stanford.edu

data. Consequently, migration of data with a hybrid of traditional survey-sinking methodology becomes possible. The method can use different source and receiver wavefield velocities, which permits imaging with converted waves present in most three-component earthquake records. Although this paper does not address the first issue directly, there is at least one method to successfully re-grid irregularly spaced teleseismic data to a regular mesh (Curry, 2003).

I begin with a general discussion of what source and receiver wavefields mean in the context of teleseismic imaging. I develop modified double square root operators appropriate for downward continuing teleseismic data, and discuss the choice of velocities required to image different converted modes. The method is then applied to a synthetic data set generated by finite differencing plane wave sources through a simplified lithospheric subduction zone model.

METHODOLOGY

The first stage in generating the migration algorithm is to develop an analytic expression for the propagation of source wavefields through the earth. To do this, two approximations are employed. First, I assume that earthquake wavefronts at teleseismic distances (between 30° and 103° in epicentral distance from source) can be approximated by plane waves. This approximation holds because at these distances and array lengths there is little curvature in the earthquake wavefront. The second approximation is that the source propagates through a vertically-stratified, v(z) medium. This approximation is consistent with the notion that earth structure 'visible' at teleseismic frequencies (i.e. between 0.005 and 4 Hz) is predominately v(z). Accordingly, the source wavefront is parameterized with constant horizontal ray parameters in a Cartesian system. This enables an analytic calculation of the planar source wavefield at all times. When discussing the source wavefield henceforth, I am referring to its analytic expression.

To enable the use of the survey-sinking algorithm, teleseismic data need to be reconfigured to an approximate equivalent of zero-offset geometry. One way that this can be achieved is to exploit the fact that planar teleseismic wavefields sweep across recording arrays in a linear fashion. This leads to a LMO of first arrivals in the recorded teleseismic section, with the degree of moveout being dependent on the incident wave's orientation to the strike of the array, as shown in Figure 1. Thus, as an initial approximation, I apply an adjoint LMO operator to remove the LMO recorded in the data. (The processing flow is depicted in Figure 2).

In this new reference frame, zero time is defined by the arrival of the teleseismic source at each station. Since all arrivals now occur at zero-time, this may be considered as a zero-offset experiment. Note that reflections and mode conversions (i.e. P- to S-wave) from horizontal discontinuities are flattened by this transformation. One drawback, though, is that diffracted hyperbolas symmetric in the initial reference frame are now skewed to one side of the hyperbola apex. The degree to which they are skewed is dependent on the angle of the applied adjoint LMO (see Figure 3). While this may not be an optimal physical representation, two observations support the use of this approximation. First, coherent events observed in the re-

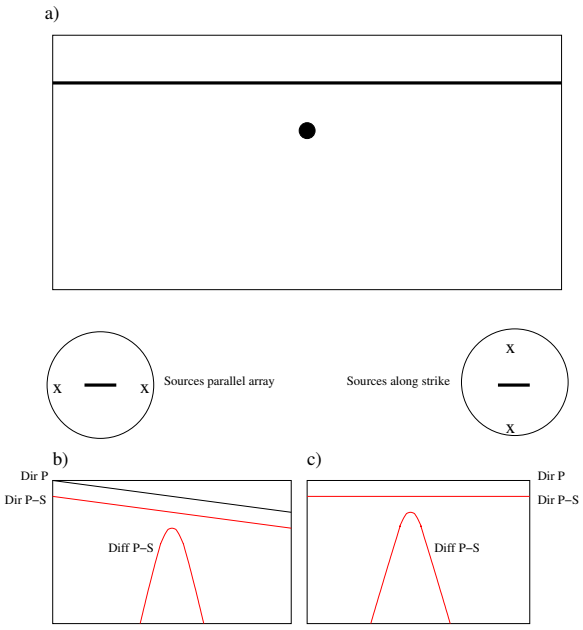

Figure 1: Diagram of a simple teleseismic scattering model. a) Earth model consisting of a planar discontinuity and point scatterer. b) P-S forward-scattering expected for a source parallel to receiver array-axis. Conversions are parallel to the source wavefront, and the diffraction is symmetric about the scattering point. c) As in b) but with source located perpendicular to receiver array-axis. jeff1-Geometry [NR]

ceiver wavefield predominately consist of planar reflected and converted events. These types of scattered energy are properly migrated by a zero-offset wave-equation method. Second, little-to-no LMO shift is applied to plane waves arriving from directions nearly or exactly coincident with the strike-axis of the recording array. In these cases planar events (plus diffractions if present) are properly migrated by a zero-offset algorithm.

Double square root equations for teleseismic geometry

The theory developed here is similar to the traditional survey-sinking migration approach where the source and receiver wavefields are downward continued into the earth (Claerbout, 2001). However, in the traditional application of zero-offset survey sinking downward continued source wavefields do not have an intrinsic initial horizontal velocity. In the teleseismic case, planar teleseismic sources nearly always have non-zero horizontal velocities. This discrepancy is reconciled by deriving modified survey-sinking equations.

To help conceptualize the equations required for this context, consider a reference frame

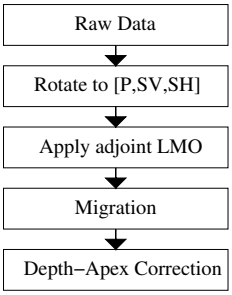

Figure 2: Processing Flow. jeff1-Flow [NR]

moving with a horizontal velocity equal to that of the source wavefield. In this reference frame a dipping plane wave propagates vertically. Hence, the downward continuation operators applied to recorded teleseismic data must transform to the double square root equations in a reference frame moving with a horizontal velocity equal to that of the source. To enable source horizontal propagation, wavefields downward continued to the next depth step are now dependent on horizontal position (x) in addition to depth (z). That is,

$$\mathrm{d}t = \mathrm{d}t(x_g, z_g, x_s, z_s), \tag{1}$$

where subscripts s and g correspond to source and receiver wavefields, respectively. To begin the derivation the differential is expressed explicitly,

$$\mathrm{d}t = \frac{\partial t}{\partial x_g}\mathrm{d}x_g + \frac{\partial t}{\partial z_g}\mathrm{d}z_g + \frac{\partial t}{\partial x_s}\mathrm{d}x_s + \frac{\partial t}{\partial z_s}\mathrm{d}z_s, \tag{2}$$

where partial derivatives with respect to the x and z coordinates may be readily associated with wavefield parameters. In a $v(z)$ medium the constant horizontal slowness of the source wavefield, p, is defined by

$$\frac{\partial t}{\partial x_s} = p, \tag{3}$$

the vertical slowness of source wavefield by

$$\frac{\partial t}{\partial z_s} = \sqrt{\frac{1}{v_s^2} - p^2}, \tag{4}$$

the variable horizontal slowness of the scattered receiver wavefield, p_{scat}, by

$$\frac{\partial t}{\partial x_g} = p_{scat}, \tag{5}$$

and the vertical slowness of receiver wavefield by

$$\frac{\partial t}{\partial z_g} = \sqrt{\frac{1}{v_g^2} - p_{scat}^2}, \tag{6}$$

where v_s and v_g represent the source and receiver wavefield velocities, respectively. Differential pairs $\mathrm{d}x_g$ and $\mathrm{d}z_g$, and $\mathrm{d}x_s$ and $\mathrm{d}z_s$ are linked geometrically by

$$\mathrm{d}x_g = \tan\theta_g \mathrm{d}z_g, \tag{7}$$

and

$$\mathrm{d}x_s = \tan\theta_s \mathrm{d}z_s, \tag{8}$$

where θ_s and θ_g represent angles of the source and receiver propagation direction with respect to the z-axis, respectively. Replacing trigonometric expressions in equations (7) and (8) with ray parameter equivalents, and by downward continuing the source and receiver wavefields by equal depth steps (i.e. $\mathrm{d}z = \mathrm{d}z_g = \mathrm{d}z_s$) one may rewrite equation (2) as

$$\frac{\partial t}{\partial z} = \frac{p^2 v_s}{\sqrt{1 - p^2 v_s^2}} + \frac{\sqrt{1 - p^2 v_s^2}}{v_s} + \frac{p_{scat}^2 v_g}{\sqrt{1 - p_{scat}^2 v_g^2}} + \frac{\sqrt{1 - p_{scat}^2 v_g^2}}{v_g}. \tag{9}$$

Equation (9) demonstrates that the effects of the propagating source wavefield are transferred to the receiver wavefield. Accordingly, using the chain rule and algebraic manipulation, the partial derivative of the receiver wavefield, U, with respect to depth is

$$\frac{\partial U}{\partial z} = \frac{\partial U}{\partial t}\frac{\partial t}{\partial z} = \left(\frac{1}{v_s\sqrt{1-p^2v_s^2}} + \frac{1}{v_g\sqrt{1-p_{scat}^2v_g^2}} \right) \frac{\partial U}{\partial t}. \tag{10}$$

Relating Fourier domain variables to the angular components of the individual plane waves

$$p_{scat}(v_g(z)) = \frac{sin\theta_g}{v_g} = \frac{k_x}{\omega}, \tag{11}$$

and applying a Fourier Transform over the temporal coordinate in equation (10) yields

$$\frac{\partial U}{\partial z} = -\mathrm{i}\omega \left(\frac{1}{v_s\sqrt{1-p^2v_s^2}} + \frac{\omega}{v_g\sqrt{\omega^2-k_x^2v_g^2}} \right) U. \tag{12}$$

The solution to differential equation (12) expressed in a discrete sense is,

$$U(z+\Delta z,\omega,p) = U(z,\omega,p) \;\; \exp\left[-\mathrm{i}\omega\Delta z \left(\frac{1}{v_s\sqrt{1-p^2v_s^2}} + \frac{\omega}{v_g\sqrt{\omega^2-k_x^2v_g^2}} \right) \right]. \tag{13}$$

With this expression, the receiver wavefield is downward continued and the image of the reflector at each model point (x,z) constructed through the usual imaging condition (Claerbout, 1971),

$$I(x,z) = \sum_{\omega} U(s=x,g=x,z,\omega). \tag{14}$$

Although the method derived here is strictly for 2-D geometry, it may be extended to account for out-of-plane propagation by assuming an underlying 2-D medium and accounting for the effects of 2.5-D propagation through incorporation of the invariant cross-line horizontal slowness. This method is also potentially applicable in 3-D, but this is not explored here.

Apex correction due to LMO shift

The LMO operation leads to vertical time shifts in the data that incorrectly position the scattering point horizontally. Figure 3 illustrates the kinematics of the LMO operation. In Figure 3, a light gray line connects the energy scattered from the discontinuous structure shown in Figure 1 with the associated source point on the incident wavefront. As illustrated in Figure 3b, after the LMO operation the scattering point must be shifted horizontally so that it falls beneath the corresponding source point on the source wavefront. This is a requirement of zero-offset migration. Noting that the relationship between the horizontal change in apex location, $\mathrm{d}x_{apex}$, as a function of depth, dz is,

$$\mathrm{d}x_{apex} = \tan\theta_s \mathrm{d}z, \tag{15}$$

the required horizontal shift operator is derived by evaluating a Fourier transform ($\mathcal{F}$) of the vertical component of velocity from depth z to the surface,

$$\mathcal{F}\left(\delta(x-x_0)\right) = \mathcal{F}\left(\delta(x - \int_0^z dz \frac{p v_s}{\sqrt{1-p^2 v_s^2}})\right) = \exp\left(-ik_x \int_0^z dz \frac{p v_s}{\sqrt{1-p^2 v_s^2}}\right). \quad (16)$$

Note that equation (16) is dependent solely on the $v = v(z)$ velocity profile and can be applied either pre- or post-migration. I have chosen to apply this shift post-migration (Figure 2)

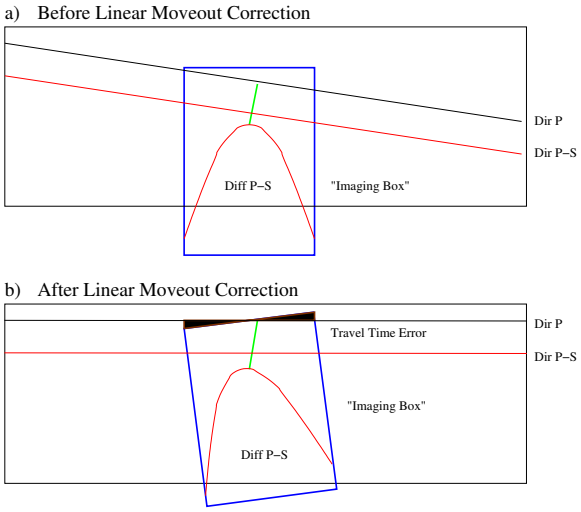

Figure 3: Diagram of LMO transform to approximate equivalent zero-offset section. a) Before LMO correction hyperbola is symmetric about the scattering point. The light gray line links points of scattered energy to the location on the wavefront causing scattering. b) After the LMO correction the hyperbola and 'Imaging box' are skewed. In-filled area illustrates the travel-time error introduced by LMO operation. Note that the hyperbola apex has zero error. The tilted light gray line shows the non-centered location of apex hyperbola. This line needs to be straighted out through a horizontal shift so that it falls beneath the scattering point. jeff1-Rotation [NR]

Velocities

In the theory developed above, there is an allowance for differing source and receiver wavefield velocities (v_s and v_g). This occurs with different wavefield scattering modes. Figure 4 illustrates the primary elastic scattering modes arising in teleseismic imaging for an incident planar P-wave source. In the forward-scattering scenario, two modes arise when the incident wavefront refracts/converts from a given scattering point. The same incident P-wavefront also reflects/converts downward from the free-surface and then reflects/converts upward from the same scattering point. Accordingly, backscattering gives rise to four in-plane scattering modes (plus one out-of-plane SV to SH scattering mode; see Table 1).

To represent the difference in propagation direction of source wavefronts in the forward- and backscattering scenarios, a negative velocity is used. That is, for forward- and backscattering, velocities of opposite and like sign are used, respectively. This is the equivalent of

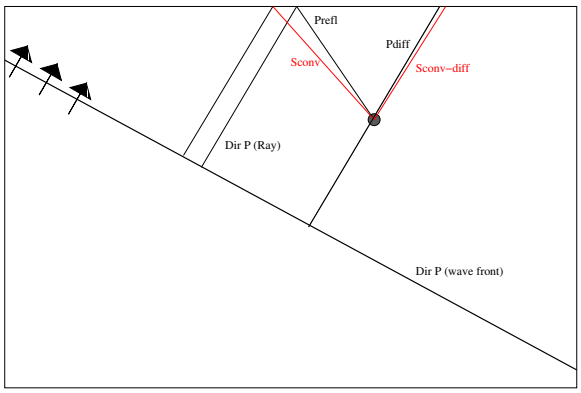

Figure 4: Diagram of primary scattering elastic scenarios in teleseismic imaging. Incident P-wavefront directly refracts/converts from a scattering point, but also may reflect/convert downward from the free-surface and then reflect/convert upward from the scattering point. Legs spent as P- and S-waves are drawn in black and light gray, respectively jeff1-Modes [NR]

choosing to take the complex conjugate of both the source and receiver wavefields in the forward-scattering scenario (Claerbout, 1971). Table 1 in the Appendix A gives the velocities used for all six primary elastic scattering modes.

SYNTHETIC MODEL AND DATA

The idealized lithospheric suture model, shown in Figures 5a and 5b, is defined on a 300×120 km^2 section and consists of three materials with differing elastic properties. A low-velocity crustal layer (white) overlies a faster upper mantle (gray). (See Table 2 in the Appendix A for model velocities and densities). At the location of the suture, crustal material from the lithospheric block to the left bifurcates, with the lower segment descending into the mantle. At a depth of $\sim$40 km, this relict (black) converts to velocities and density higher then the surrounding mantle (note the proportionally greater increase in *S*-velocity) and thereafter folds and thins to the right of the model.

Several sets of two-component seismograms were computed through the lithospheric model using a 2-D, elastic pseudo-spectral code (Kosloff et al., 1990). The seismograms comprise a suite of plane *P*-wave sources interacting with the model over a range of incident horizontal slowness, p = [0.05, -0.05, 0.06, -0.06, 0.07, -0.07] s km^{-1}. The output seismogram sections consist of 120 traces computed at 3km intervals at the free surface.

One preprocessing requirement is that a reasonable zero time mark is computed for all traces. The method employed here consists of transforming raw data sections, $\mathbf{U}$=[U_1, U_3], into up-going *P*- and *S*-wavefield sections, $\mathbf{w}$=[P, SV], via the free-surface transfer matrix (Kennett, 1991). Multi-channel cross-correlation (VanDecar and Crosson, 1990) it then applied to a window about the direct *P*-arrival to allow optimal alignment of wavefield sections. A representative set of synthetics seismograms is presented in Figures 5c and 5d. Generally, the two sections are characterized by a combination of spectral sub-planar reflectors, and diffractions from the higher (spatial frequency) wavenumber model structure.

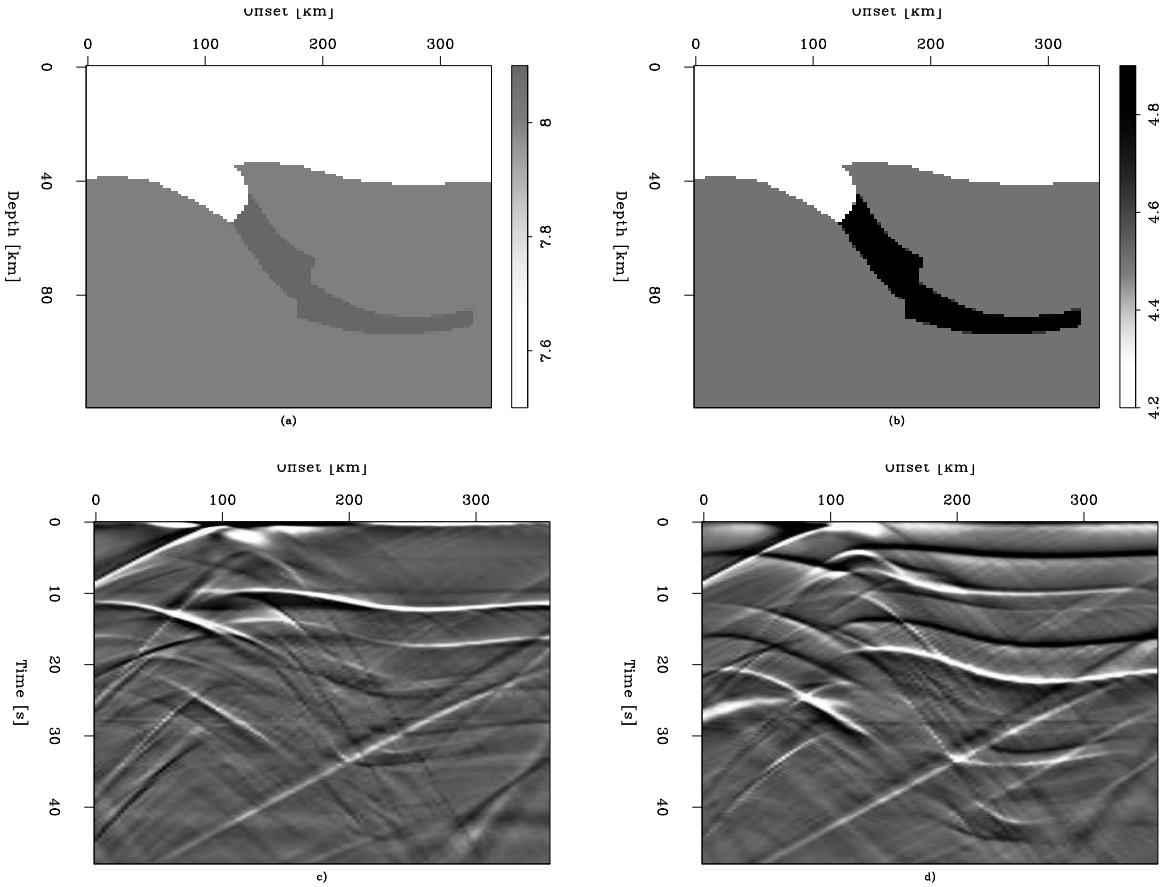

Figure 5: Idealized, three material collisional suture model and representative finite difference data. a) P-velocity model (Velocities and densities of each material are given in Table 2); b) S-velocity model; c) Sample processed synthetic section from model in a) and b) rotated into P wave vector; d) As in c) but rotated SV wavefield. jeff1-Figure4 [ER]

EXPERIMENTS

The results of applying the hybrid survey-sinking algorithm to the synthetic data set are presented in this section. The $v(z)$ velocity profiles used in these migrations consist of a 40-km-thick crust overlying an upper mantle half-space. The values of the P- and S-wave velocities employed are given in the first two rows of Table 2.

Figure 6a presents the forward-scattered P-S migration result for the SV component shown in Figure 5c where the source is incident from the right. Both the crust-mantle (white-to-gray in model) and relict crust-mantle (black-to-gray in model) discontinuities are well imaged, but the crust-relict crust (white-to-black in model) boundary is notably absent due to weak amplitudes of incidence-angle dependent P-S conversions. Figure 6b presents the backscattered P-P migration result for the P-wave component presented in Figure 5d. The structure imaged in this case is predominantly the crust-mantle discontinuity. This is expected since the magnitude of the P-P reflection coefficient for the mantle-relict crust discontinuity is very weak as

the change in P-wave velocity is less than two percent. Also note the vertical mis-positioning of structure in Figures 6a and 6b arising due to use of a $v(z)$ reference model.

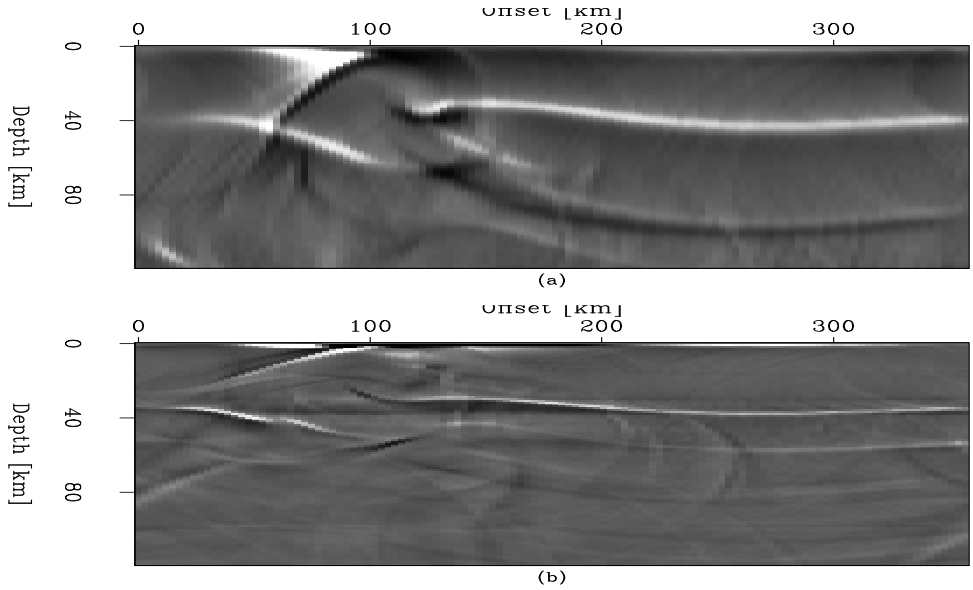

Figure 6: Results for applying migration algorithm to data shown in Figures 5c and 5d. (a) Forward-scattered P-S image; (b) Backscattered P-P image. jeff1-Figure5 [ER]

Figure 7 presents the results of stacking the migrations of all 6 generated events for 4 of the 6 primary elastic scattering modes. Results show good reconstruction of the crust-mantle discontinuity. Panels (a), (c) and (d) also exhibit recovery of the relict crust, though with differing relative amplitudes. Forward-scattered P-S and backscattered P-P (Panels a) and b)) do not suffer from cross-mode contamination to the same degree as modes in panels c) and d). This is attributed to these two modes being the first scattered arrivals in their respective wave sections. These modes are themselves separated by the orthogonality of waves ending in P- and S-phases.

Forward-scattered P-P and backscattered S-P images are not shown since they are severely degraded. Forward-scattered P-P energy has little-to-no sensitivity to travel-time variations since the scattered wavefield moves at the same velocity and in the same direction as the source wavefield. This yields small-to-zero time delays insufficient for acceptable resolution of model structure. Backscattered S-P energy is twice converted and, over the range of angles considered here, has a much lower amplitude relative to the earlier arriving P-P energy.

CONCLUSIONS

The application of an adjoint LMO operator to teleseismic data successfully transforms recorded teleseismic wavefields to an approximate equivalent to traditional zero-offset. This transformation enables the use of zero-offset migration techniques. The hybrid survey-sinking method developed here downward continues all primary elastic scattering modes, and produces interpretable images.

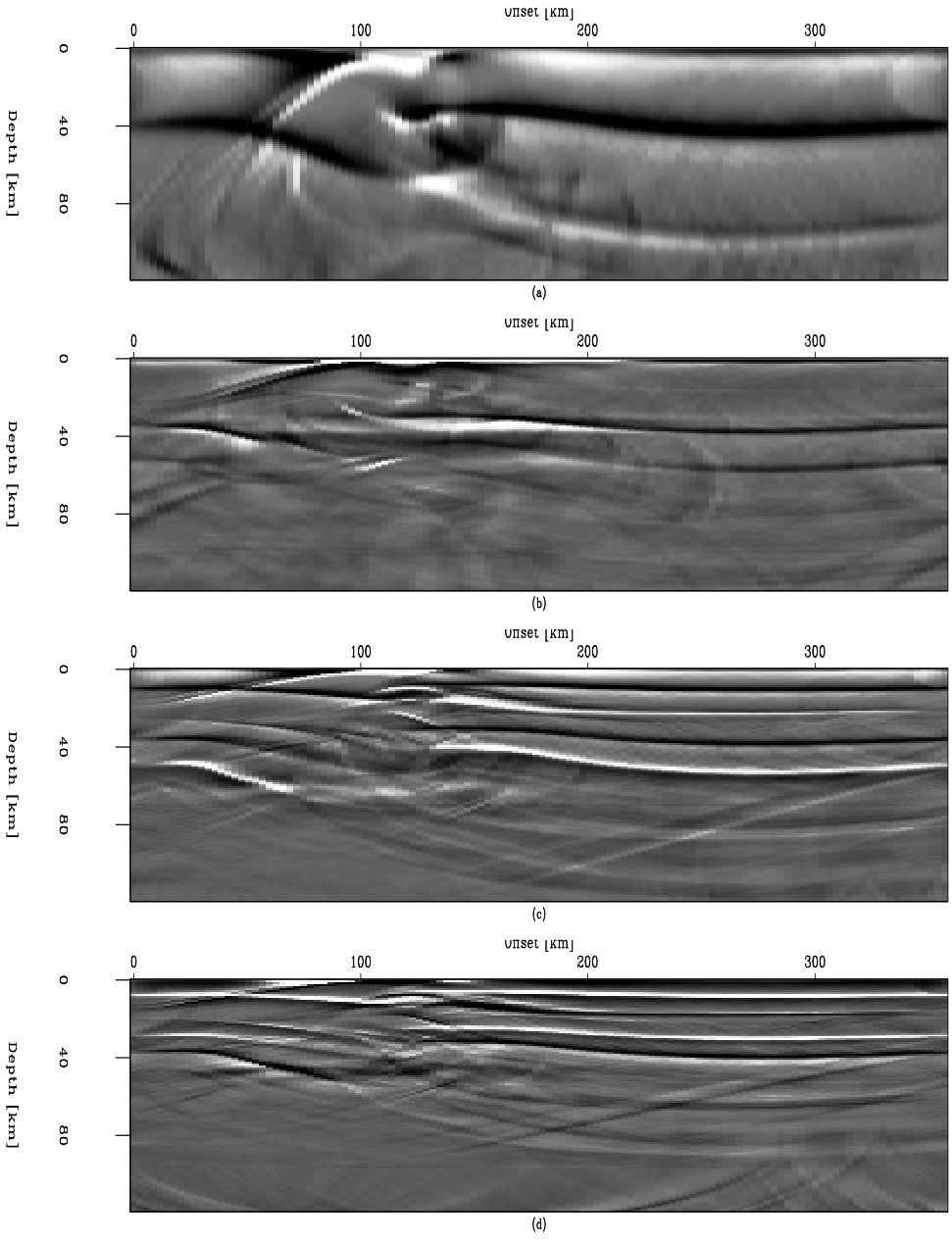

Figure 7: Stack of all events for given scattering modes. a) P-S forward-scattering; b) P-P backscattering; c) P-S backscattering; and d) S-S backscattering. jeff1-Figure6 [ER]

Migration results for the lithospheric test model show a good recovery of the model structure. The absense of some model structure in the images is attributed to a combination of poor illumination and weak scattering amplitudes. Imaged discontinuities are slightly displaced from their true locations due to the $v(z)$ velocity model used. In addition, diffractions do not collapse perfectly back to point-like scatterers. The general success of the derived zero-offset survey-sinking methodology and the possibility of undertaking more advanced analysis of angle-dependent scattering behavior further motivate the study of wave-equation imaging of teleseismic data (Shragge and Artman, 2003).

REFERENCES

Bostock, M. G., Rondenay, S., and Shragge, J., 2001, Multiparameter two-dimensional inversion of scattered teleseismic body waves - 1. theory for oblique incidence: Journal of Geophysical Research, **106**, 30771–30782.

Claerbout, J. F., 1971, Toward a unified theory of reflector mapping: Geophysics, **36**, no. 03, 467–481.

Claerbout, J., 2001, Basic earth imaging: Stanford University.

Curry, W., 2003, Iteratively re-weighted least-squares and PEF-based interpolation: SEP–**113**, 379–390.

Kennett, B. L. N., 1991, The removal of free surface interactions from three-component seismograms:, **104**, 153–163.

Kosloff, D., Kessler, D., Filho, A. Q., Tessmer, E., Behle, A., and Strahilevitz, R., 1990, Solution of the equations of dynamic elasticity by a Chebychev spectral method: Geophysics, **55**, no. 06, 734–748.

Shragge, J., and Artman, B., 2003, Imaging with buried sources: SEP–**113**, 157–162.

VanDecar, J. C., and Crosson, R. S., 1990, Determination of teleseismic relative phase arrival times using multi-channel cross correlation and least squares: Bulletin Seismological Society of America, **80**, 150–169.

APPENDIX A

Table 1. Velocities used for different scattering modes (α and β are P- and S-wave velocities, respectively).

Scattering Mode Index	Scattering Mode	$\check{v}$	$\hat{v}$
1	FS P-P	α	α
2	FS P-S	α	β
3	BS P-P	$-\alpha$	α
4	BS P-S	$-\alpha$	β
5	BS S-P	$-\beta$	α
6	BS S-S	$-\beta$	β

Table 2. Lithospheric Model Parameters.

Parameter	P-wave velocity (km s^{-1})	S-wave velocity (km s^{-1})	Density (g cm^{-3})
Crust	6.2	3.6	2.8
Mantle	8.0	4.5	3.2
Relict Crust	8.1	4.9	3.3